Measurement of the effect of water droplets on strained laminar flames using two-phase PIV

Luming Fan[a,*], Cheng Tung Chong[b,c], Kenji Tanno[a,d], Dante McGrath[a], Yutao Zheng[a], Simone Hochgreb[a]

[a] *Hopkinson Laboratory, Department of Engineering, University of Cambridge, Trumpington Street, CB2 1PZ, United Kingdom*
[b] *China-UK Low Carbon College, Shanghai Jiao Tong University, 201306 Lingang, Shanghai, China*
[c] *School of Mechanical Engineering, Faculty of Engineering, Universiti Teknologi Malaysia, 81310, Skudai, Johor, Malaysia*
[d] *Central Research Institute of Electric Power Industry, 2-6-1 Nagasaka, Yokosuka 240-0196, Japan*

Abstract

The effect of water droplets on strained methane-air laminar flames is investigated using particle image velocimetry of both gas and liquid phases. We use the impinging flame configuration to measure the laminar flame speed (gas) as well as the motion of the liquid phase, simultaneously. Water droplets of mean diameter 36.6 μm are produced by an ultrasonic atomizer and dispersed in a methane/air flow, for a constant molar ratio (12–36%) to the fuel (methane). This corresponds to a water mass fraction of 0.8–2.2% at stoichiometry. The slip motion between gas phase and droplets is quantified by seeding 1.7 μm mean diameter oil droplets into the reactant flow, and using an image segmentation method to determine the velocity of the gaseous flow and water droplets separately. The result reveals a clear slip velocity between the two phases: the inertia of relatively large droplets results in

*Corresponding author:
Email address: luming.fan@outlook.com (Luming Fan)

Preprint submitted to 38th international combustion symposium, supplementary material included

a drift into the flame front at a higher speed than the gaseous flow, by a factor of 10-30% in most cases. Measurements of the gas-phase flow show that the addition of water droplets significantly reduces the reference flame speed, especially at high strain rates. However, numerical simulation on water vapor addition under the same condition only predicts a slight drop in the reference flame speed, suggesting water droplets are more effective in flame suppression than vapor. This is the first time that the two-phase PIV technique has been applied to solve a problem in combustion investigations. We validate this technique under a non-reacting impinging flow prior to the flame experiment, and report the strategies adopted for better image quality and subsequently easier segmentation between oil and water droplets. The technique can be next applied to measure the slip velocity for volatile fuel sprays, where the slip motion plays an important role in determining both their evaporation rate and residence time in a flame.

Keywords: water droplet, flame suppression, slip velocity, two-phase PIV, image segmentation

---

1. Introduction

Water sprays have been widely used as a fire suppressant, particularly since halon compounds have been banned due to environmental concerns. A considerable number of experiments on fire suppression by water-mist have been conducted during the past two decades, for example [1, 2]. Many of these studies concluded that due to large latent heat of vaporization, the inhibition effect of water droplets were comparable or even better than gas suppressants. Current water sprinkler systems installed in buildings produce large water droplets (> 100 μm) with a high momentum. However, many researchers believe that finer water droplets can be more effective in fire suppression as they have a longer settling time, and thus can stay in the reaction zone for longer. Hence, progress has also been made in understanding the mechanisms of droplets as suppressants, including size and composition. In a series of studies by Chelliah and co-workers [3, 4], water droplets with metal salt or alkali additives were found to be more effective in flame suppression than pure water.

Quantitative analyses on droplet dynamics and its effect on prototypical laminar flames have been explored by Continillo and Sirignano [5], Chelliah and Lentati [6, 7], Chen and Rogg [8], and Kee *et al.* [9]. These models have produced useful predictions on the effect of droplet size, thermal properties, residence time on non-premixed counterflow flames, but related experimental data is limited to the observations in [3] regarding the effect of droplets on the extinction strain rate of premixed and non-premixed flames.

The geometric configuration of impinging or counterflow premixed flames has been proven to be a useful paradigm in combustion, anchoring models of flamelets and the effect of composition and strain on the flame burning rate (e.g. [10]). In these studies, the strain rate is obtained from the radial velocity profiles, and the reference

flame burning velocity is obtained from the minimum axial velocity upstream of the flame. In the present paper, we extend this experimental configuration to include the presence of controlled droplet mists in a stabilized stretched methane-air flame, to investigate their effects on the burning velocity. However, a significant issue arises regarding the difference in velocity between droplets and surrounding gas. The strain and reference gas flow velocities can still be used as a reference, but they are different from the droplet velocities, which determine the local droplet number density for a constant flux, and the droplet residence time in the reaction zone.

In the present study, we use two-phase particle image velocimetry (PIV) based on image segmentation to resolve the velocity of both gas and dispersed phases (water droplets) simultaneously. In this method, Mie scatter signals from both large droplets and micron-sized particles are recorded by the same camera, which are then separated by using algorithms based on the intensity differences, particle image size, shape, or their combinations. An example of the algorithm using image segmentation method can be found in [11]. This technique has been used in demonstrative PIV studies for the separation of droplet and gas velocity in non-reacting flows. Apart from the image segmentation method, an alternative technique is the use of laser-induced incandescence for particle image velocimetry (LII-PIV) [12], which allows two-color separation of phases. A companion paper discusses the potential use of LII-PIV for the present experiment as well [13].

In the present study, we use a stagnation flame configuration as in [2], and test a methane/air premixed flame seeded with 36.6 μm water droplets. The image segmentation method is adopted to discriminate water droplets and 1.7 μm oil aerosol, which are simultaneously seeded into the flow. Particle images of water are used to determine the velocity field of the dispersed phase, and those of oil is used to extract the gas flow velocity. The difference in reference velocity with and without droplets

characterizes the change in the burning velocity at a given strain rate. Solid tracers such as alumina could not be used for gas phase seeding in this experiment, as for the given flow rates the seeder particle delivery rate was not sufficiently stable for the image segmentation method. The following sections introduce the experimental setup, image processing method, a validation in cold impinging flow, and finally the flame speed results for both phases.

2. Experimental setup

2.1. Burner and flow delivery system

Figure 1 illustrates the experimental setup. The stagnation burner consisted of a 70 mm diameter chamber, with a height of 260 mm, which converged to an aerodynamically shaped nozzle of 22 mm exit diameter shrouded by a 5 mm wide annular nitrogen co-flow. A water-cooled brass plate provided the impingement surface 20 mm above the nozzle. An ultrasonic fluid surface breakup atomizer (SonoTek 120-1009) was installed at the bottom of the burner for generating water droplets. This was the same type of atomizer used in Chelliah and co-workers' study [4], but with a different nozzle length (lower resonance frequency), which can produce larger droplets. The primary advantages of using an ultrasonic fluid breakup nozzle over the traditional air-blasting ones are that they do not produce flow disturbances, and that the droplet size distribution is relatively compact, which facilitates the image segmentation. The water delivery was controlled by a syringe pump with 0.5% precision. A bypass air flow was set to produce olive oil aerosols through an air-blast atomizer. The flow was forced through an impactor chamber with multiple baffles inside before mixing with methane and air, which removed large oil droplets that cannot follow the sharp velocity gradients. The oil injection rate was set to 0.03-0.06

mL/min, corresponding to 0.05% of total mass flow rate and 0.18% of total energy. Hence the oil aerosol is expected to have minimal effect on the two-phase flame.Oil droplets may disappear by 600 K based on estimated flash point temperatures. For oil seeded PIV in flames, there are typically least 1-2 velocity vectors appearing downstream of a minimum axial velocity, which also suggests that oil particles survive the early flame temperature rise, and that the reference flame speed was captured. The ability of the oil droplets to follow the flow was validated by a comparison with a test in which 0.5 μm alumina particles were instead used for methane flame speed measurement at the same condition. A Dantec phase doppler anememometer (PDA) was used to measure the water droplet and oil aerosol size distribution separately at 1 mm height above the burner exit.

The relatively large size of water droplets means that not all droplets reached the burner exit but were instead collected at lower points in the setup. To account for the loss, we conducted calibrations with various air and water flow rates. After running the system for 30 minutes, residual water together with the ceramic beads were carefully collected and weighed by a micro-scale. It was found that only 60% of the injected water actually left the burner. This fraction was consistent for various flow conditions, and comparable to the measurements in [4] (about 70%) for a similar atomizer and burner configuration. By conducting the same calibration test multiple times, the uncertainty is estimated to be less than 5%. The water loading mentioned in the paper are values determined after correction.

2.2. Two-phase PIV system

Three requirements need to be satisfied for the image segmentation method beyond those for normal PIV: (a) the spatial resolution must be high enough, so oil and water droplets are sparsely dispersed on the image; (b) the seeding density of

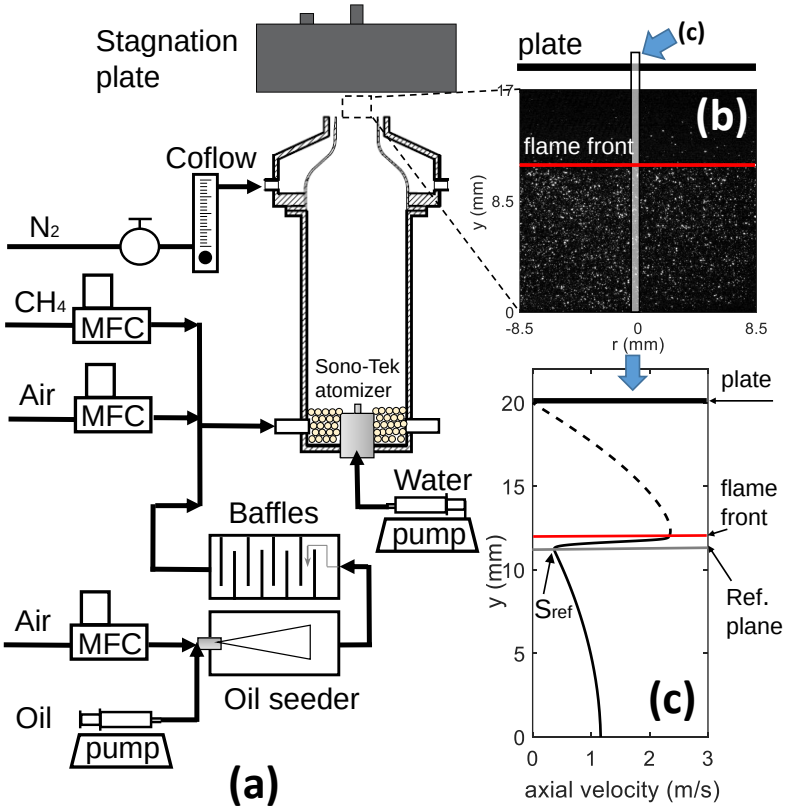

Figure 1: (a) experimental setup, (b) an example PIV image, and (c) a schematic axial velocity profile.

both oil aerosol and water droplets must be moderate, so that individual droplet images can be detected and separated; and (c) the laser fluence should be uniformly distributed so that the intensity of individual spots has a strong correlation only with the droplet size, rather than its location. In order to fulfil these requirements, a 532 nm PIV laser was used to generate a non-diverging light sheet by expanding the beam through a focal length, FL = -25 mm concave cylindrical lens followed by a FL = 150 mm convex lens. The height of the laser sheet formed after this lens combination was roughly 60 mm. A slit was installed to trim the side wings of the Gaussian laser profile in both vertical and out-of-plane directions to make sure that

the laser fluence is uniformly distributed in the illumination volume. Another FL = 500 mm convex lens was set after the slit to reduce the thickness of the laser sheet. The final light sheet was 20 mm in height and 0.5 mm thick. The energy at the test section for both pulses was set to 5 mJ so as to guarantee sufficiently strong Mie scatter signal for the fine oil droplets, but not to damage the camera by scatter from water droplets.

A CCD camera was operated in double frame mode at 5 Hz to collect the Mie scatter signal from both oil and water droplets. A Nikkor 60 mm Micro-lens combined with a Sigma $\times$ 2 teleconverter was used to focus the image. They provided a very high pixel resolution at 10.2 μm/pixel. A 532 $\pm$ 5 nm filter was installed before the Micro-lens to minimize the background signal, and thus to the largest extent to facilitate the image segmentation. To record both oil and water images, the aperture size was set to $f/D = 5.6$. Under such conditions, the peak intensity of oil droplet images was roughly 300 counts, whilst the blooming spots of water droplets were overexposed. Such a large intensity and size contrast is ideal for image segmentation, but not so favourable for determining the droplet velocity vectors. Since the water droplet image acquires a top-hat profile due to pixel saturation, the usual Gaussian estimator in the vector calculation algorithm fails, and pixel-locking can occur. In order to avoid these issues, we repeated all test cases with the presence of only water droplets at an aperture size of $f/D = 16$ to avoid overexposure, so as to generate a set of images optimized for vector field calculation.

Figure 2(a) presents the droplet size PDFs measured by the PDA system. The ultrasonic atomizer generated a range of water droplet sizes from 20 to 60 μm, with an arithmetic mean diameter at 36.6 μm and SMD of 40.7 μm. The diameter range of water is clearly separated from that of oil, which has a mean diameter of 1.7 μm and a maximum about 5 μm. For PIV, the arithmetic mean diameter is more

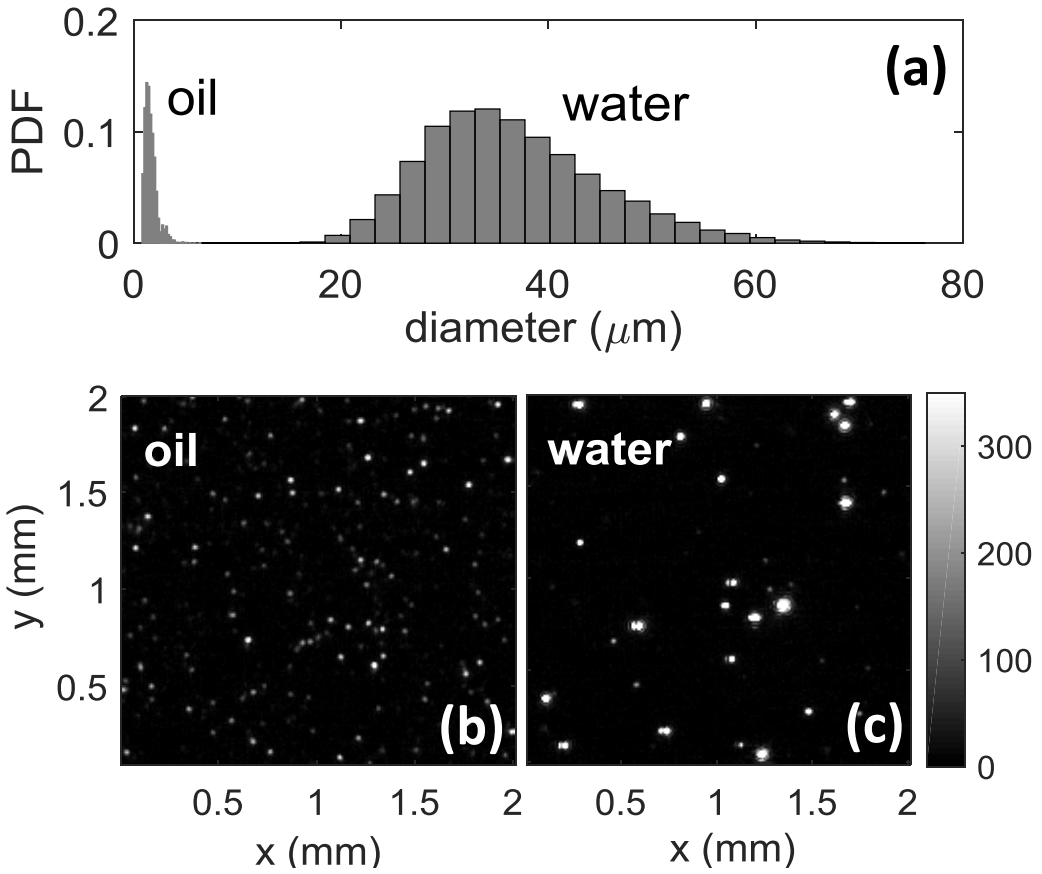

Figure 2: (a) Droplet size distribution for oil and water, each measured separately by a Dantec PDA system. Sample raw PIV image of (b) sparsely seeded oil aerosol; and of (c) water droplets.

useful than SMD, because the cross-correlation is mainly determined by the largest number of droplets moving at a similar speed, rather than the largest amount of liquid volume contained in a certain size droplet. The corresponding Stokes number for the water and oil droplets are estimated as 3.3 (larger than unity) and 0.01, respectively. Therefore, the response of water droplets is too slow to follow the flow, and as a consequence, slip motion may appear. Figure 2 (b), (c) are sample Mie scatter images of oil and of water droplets, respectively. They are very different in intensity and shape: the oil particle images are in general low intensity and smaller

than 4 pixels, whilst most water droplet images are saturated in the centre and larger than 15 pixels. Shadow particle images (a smaller particle image adjacent to the main one) can be observed on figure 2(c), which are formed due to refraction of laser light across those large water droplets.

3. Data processing

3.1. Image segmentation

Data processing was conducted using Davis 8.3 from LaVision. A size threshold (median filter) was combined with an intensity threshold to create a *mask* to separate the oil and particle images, as described further on. The median filter works better as a criterion for segmentation than the pixel intensity alone [11], because the edges of bright spots are also weak.

Figure 3 illustrates the image segmentation procedure: (a) a 15-count intensity threshold is applied for denoising the raw PIV image; (b) the PIV image is processed by a median filter with a kernel size of 8 pixels. All oil droplet images as well as the residual camera noise are removed by this median filter; (c) a 5×5 pixel Gaussian filter is applied to smooth the image; (d) the smoothed PIV is then binarized, and the resulting areas are used as masks for the original image; and finally, (e) pixels outside the masked area are set to zero. With these steps, the water droplet images are successfully separated, as shown in Fig. 3(e).

Ideally, once water droplet images have been separated, the remaining signals should correspond to oil droplets. However, Figure 2(c) shows that there are a few small but very bright water droplet images. These may be attributed to a small number of water droplet edges entering or leaving the light sheet. These signals cannot be separated from oil droplets by judging the spot size alone – the brightness

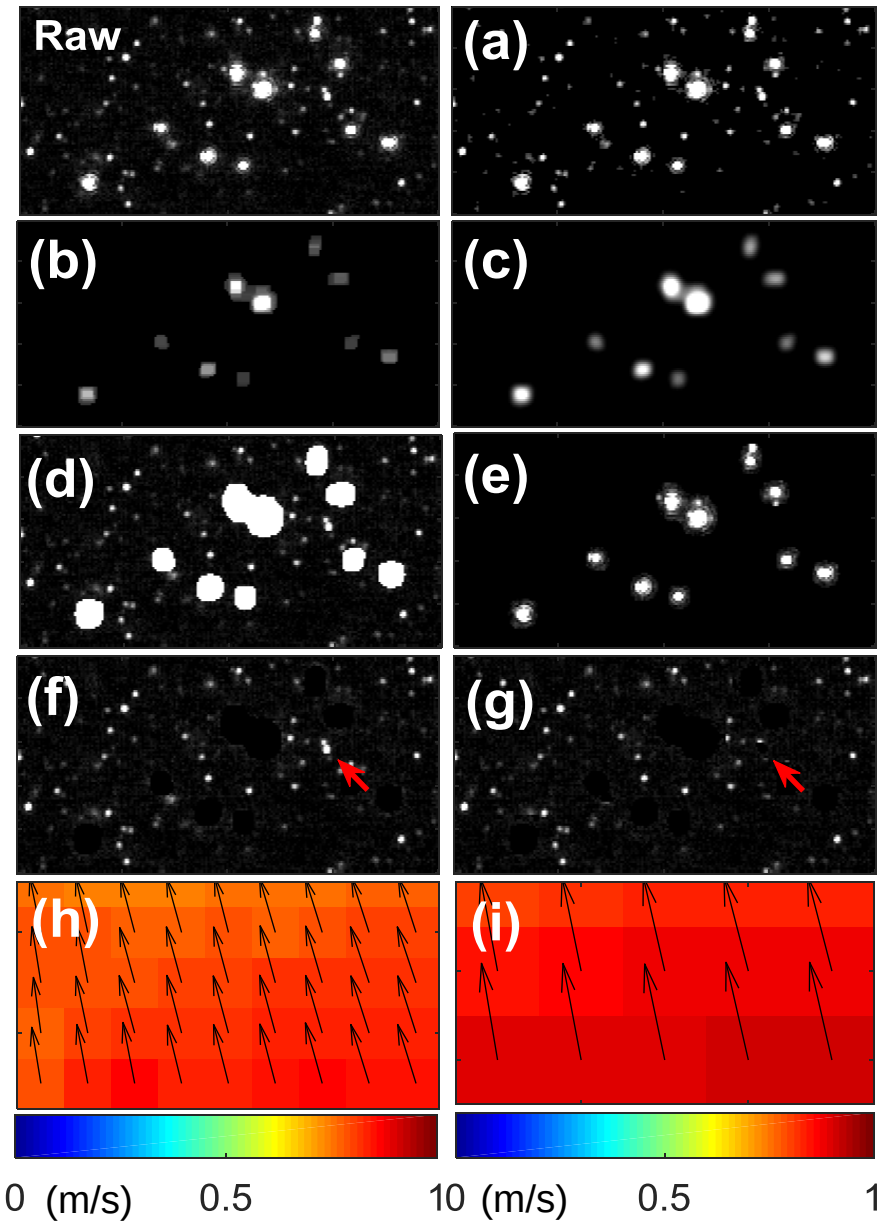

Figure 3: Data processing procedure, on a 1×2 mm^2 field. Subfigures (a)-(g) correspond to the steps described in the text. (h) and (i) are instantaneous velocity fields of gas and water droplets, respectively. Missing vectors in (i) were filled by interpolation.

should be considered as well. Hence, for extracting oil droplets, steps (a)-(e) remain unchanged, except that the median filter kernel size in step (b) is now set to 5 pixels, and that in step (e), only the signals outside the masked area are preserved (inversion of mask). (f) After the small droplet images are obtained, (g) another mask based on intensity threshold of 800 counts was applied to remove the partially illuminated water droplets. The red arrow in Fig. 3(f) and (g) marks a small but bright particle image that was removed by this operation. The oil droplet images can now be separated, as shown in Fig. 3(g).

3.2. PIV processing

Vectors were calculated based on the processed oil and water images using multipass cross-correlation with a decreasing window size. For oil droplets the window size was 64 $\times$ 64 pixels for the first pass, and 32 $\times$ 32 pixels for the second pass. A 15-count low threshold was applied for the oil PIV images to remove noise. The black holes left from the removed water droplets were then merged into the background. Since water droplets are sparser than oil, we used 128 $\times$ 128 and 64 $\times$ 64 window sizes for the first and second pass, respectively. A 25% overlap was applied when shifting the interrogation window. Vectors with a Q-factor lower than 1.2 were removed. Areas with missing vectors due to insufficient seeding were filled by interpolation. In the worst case scenario, the fill-in vector ratio for water images was 16%. Such interpolation is justifiable in our experiment since for the laminar flat flame, the velocity field upstream of the flame is expected to be smooth. Instantaneous velocity fields of gas and water droplets extracted from Fig. 3(a) are shown in Fig. 3(h) and (i), accordingly.

4. Validation in a non-reacting impinging flow

Unlike the case of two-color methods, there is no concrete evidence to tell whether all large/small droplets have been thoroughly separated after image segmentation. Therefore it is necessary to conduct validation tests in a known flow. We characterized a cold impinging flow on the same rig seeded with oil, water, and 0.5 μm alumina tracers, respectively. The test was then repeated with the mixture of oil and water droplets, and the two-phase PIV processing procedure was tested. The strain rate for this case is estimated as 110 s^{-1}.

The mean axial velocity profiles averaged over 200 single-shots are extracted from the centre line and compared in Fig. 4. The subsequent velocity profiles (circles) based on segmented images match well with their counterpart (solid lines) where only oil or only water droplets are presented. The measured velocity standard deviation for oil or alumina seeding is around 0.02-0.03 m/s, and about 0.03-0.05 m/s for water droplets. An initial slip velocity of 0.15 m/s can be identified at the burner exit $y = 0$ mm, as the converging nozzle cannot accelerate the large droplets as quickly as the gaseous flow. Once leaving the burner, the flow starts to decelerate as it approaches the impinging surface. Conversely, the large droplets show a slow response to the pressure gradient, and produce a relative slip velocity of 0.1 m/s at $y = 17$ mm. The non-reacting test result shows that the data processing procedure is effective for separating the oil and water droplets used in this study.

5. Methane/air flame laden with water droplets

The effects of water droplets on methane/air flame speed were investigated by the two-phase image segmentation PIV technique above on a stagnation flow configuration. Two different water injection rates relative to the fuel, $X_{H_2O}/X_{CH_4} =$

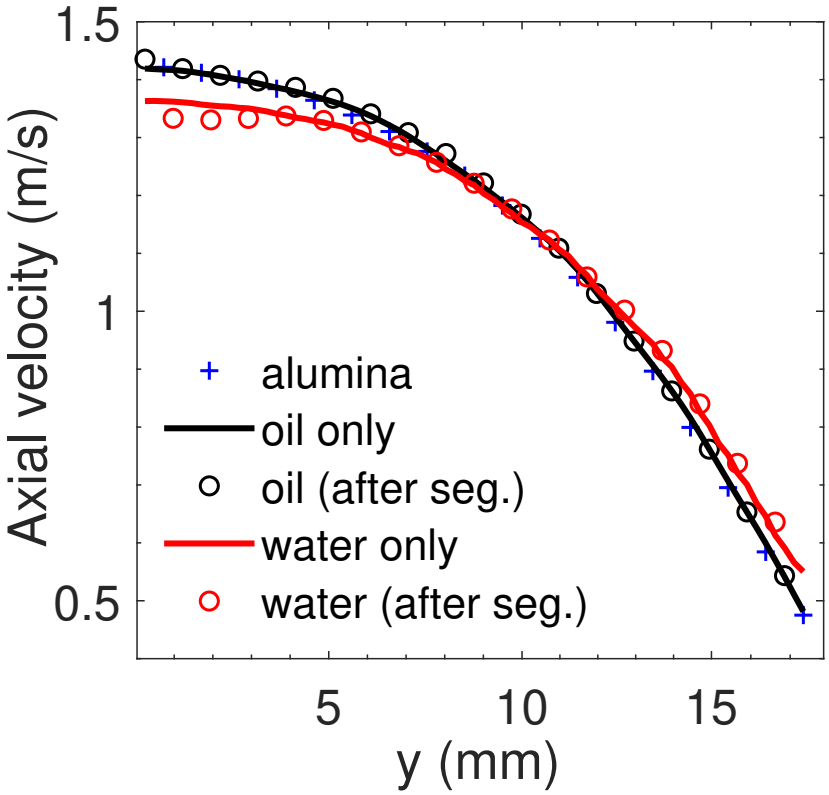

Figure 4: Validation tests on an impinging non-reacting flow of 30 slpm and 20 mm spacing between nozzle and plate. The strain rate is 110 s^{-1} in this case. The mean axial velocity is extracted from centre line for comparison. Crosses: 0.5 μm alumina tracers seeded in the gas, solid black line: oil droplets seeded in the gas, solid red lines: water droplets seeded in the gas. Black and red circles: flows seeded with both oil and water, respectively, and subsequently segregated after image segmentation. The impinging plate is located at $y = 20$ mm from the nozzle.

12% and 36% by mole were used. They are equivalent to a mass fraction of 0.8% and 2.2% (or a molar fraction of 1.1% and 3.3%) at stoichiometry. The stagnation flame method for determining the flame speed was described in detail in [10]. The strain rate was varied by changing the bulk flow rate of the mixture, from 18 to 36 slpm depending on the equivalence ratio. The equivalence ratio ranged 0.76-1.25 for 12% water, and 0.85-1.15 for 36% water. Beyond these ranges the flame cannot be sustained. The flame speeds of methane/air mixture without water droplets were

also acquired as a reference, using oil-seeded PIV.

5.1. Gas and droplet dynamics

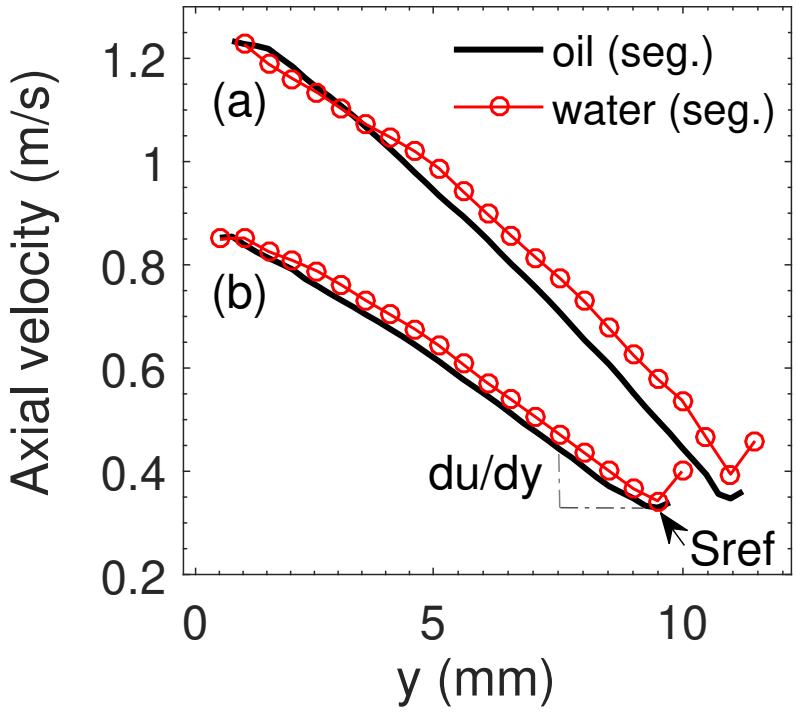

Figure 5: Sample simultaneous measurements of the axial gas and water velocity along the symmetry plane of a a stretched methane/air flame. The two sets of axial velocity profiles were obtained for (a) $\phi = 1.05$ at 31 slpm, and (b) $\phi = 0.85$ at 22 slpm. Both cases are for 12% water. The slip velocity at the reference plane is (a) 6 cm/s and (b) 1.4 cm/s, respectively. The local strain rate at the reference plane are 139 and 104 s^{-1} for the two cases.

Figure 5 shows two examples of simultaneous axial gas and water velocity measurement along the burner center line. Owing to the high spatial resolution used, the velocity gradient in each interrogation window (320 μm) was very small relatively to the overall velocity gradient. The typical velocity uncertainty at the reference plane was 0.025 m/s for both oil and water. For reacting cases, the initial slip velocity at the burner exit is not evident, as now the flame position is much closer to the

nozzle, and the flow decelerates even before reaching the exit. In most cases, for example curve (a), water droplets move faster than the gaseous flow due to larger inertia. However, in some lean cases at low flow rates, the difference between two phases is very small, as shown by curve (b), or even an opposite trend appears due to the gravitational force on the droplets. After examining the axial velocity curves under various test conditions, we find that the magnitude of the slip velocity at the reference plane is dependent mainly on the global velocity gradient. As expected, a larger slip velocity appears in cases where the gradient of axial velocity is steeper. But the slip motion is also affected by the equivalence ratio and water loading, which determines the reference flame speed and the stagnation position.

5.2. Reference flame speeds

Figure 6 shows the reference velocity S_{ref} of the gas and of water droplets at the reference plane for four cases as a function of the gas strain rate [a]. The gas strain rate is used as the x-axis for both gas and liquid phase. Since only relatively low strain rates were tested (below 180 s^{-1}), the expected heat loss effect should be minimal [10]. An automated script was written to detect the reference flame speed and the local strain rate, but the noise in the velocity measurements caused by sparse seeding led to excessive incorrect detection of the stagnation position. Hence, the results were checked frame by frame to make sure that the right position was recognized for all single shots. For the gas phase (black solid circles) and liquid phase (red solid circles) measurements, each data point was averaged over 50 single-shots. Further refinement of the algorithm would allow a larger number of images to be considered. Although pixel-locking is not expected to cause significant bias in the

[a]The full data sets are presented in the supplementary figure (Figure S1). The average flame position to the plate for each case is summarised in Figure S2.

water velocity measurement in our case, here we only use the result based on the dataset acquired separately for water with no overexposure (see Section 2.2). The baseline methane/air (no water) results are plotted as blue circles (each shows the average velocity over 30 images). The code worked well in this case due to sufficient oil seeding, so more data points were processed and presented. Since the asymptotic theory has not been validated for two-phase stagnation flows, we do not extrapolate the flame speed to zero strain rate.

The burning velocity of methane/air mixtures is substantially reduced by the addition of water droplets, as obtained by either oil (gas) and water (droplet) tracers. This is of course expected, as the flame temperature should be reduced by the heat of vaporization and higher heat capacity of the mixture. The flame front moves towards the plate when more water is added, indicating lower reference velocities. Unlike the methane/air case, the reference velocity for flames with water droplets decreases with strain, in a similar manner as the findings for a propane/air/water flame in [2]. This may be caused by the higher local droplet number density at the flame front for higher strain rates. Reference speeds S_{ref} measured by the water droplets are larger than gas velocities by 10-30% in most cases. This is a direct result of the inertia of the larger water droplets. However, for $\phi = 0.85$ and a strain rate around 100 s^{-1}, the flame speed measured by oil and by water droplets are very close, which is attributed to the low velocity gradient as illustrated by curve (b) in Fig. 5 as well as the gravitational effect. The droplet dynamics affects the residence time of the droplets in the reaction zone, which, as a consequence, must have an effect on the gaseous flame speed. Based on the acquired data, the droplet dynamics and its effects on the flame speed are further investigated numerically by two-phase counterflow models [6, 8] in an upcoming study.

Nevertheless, a comparison can be made by considering the effect of water vapor

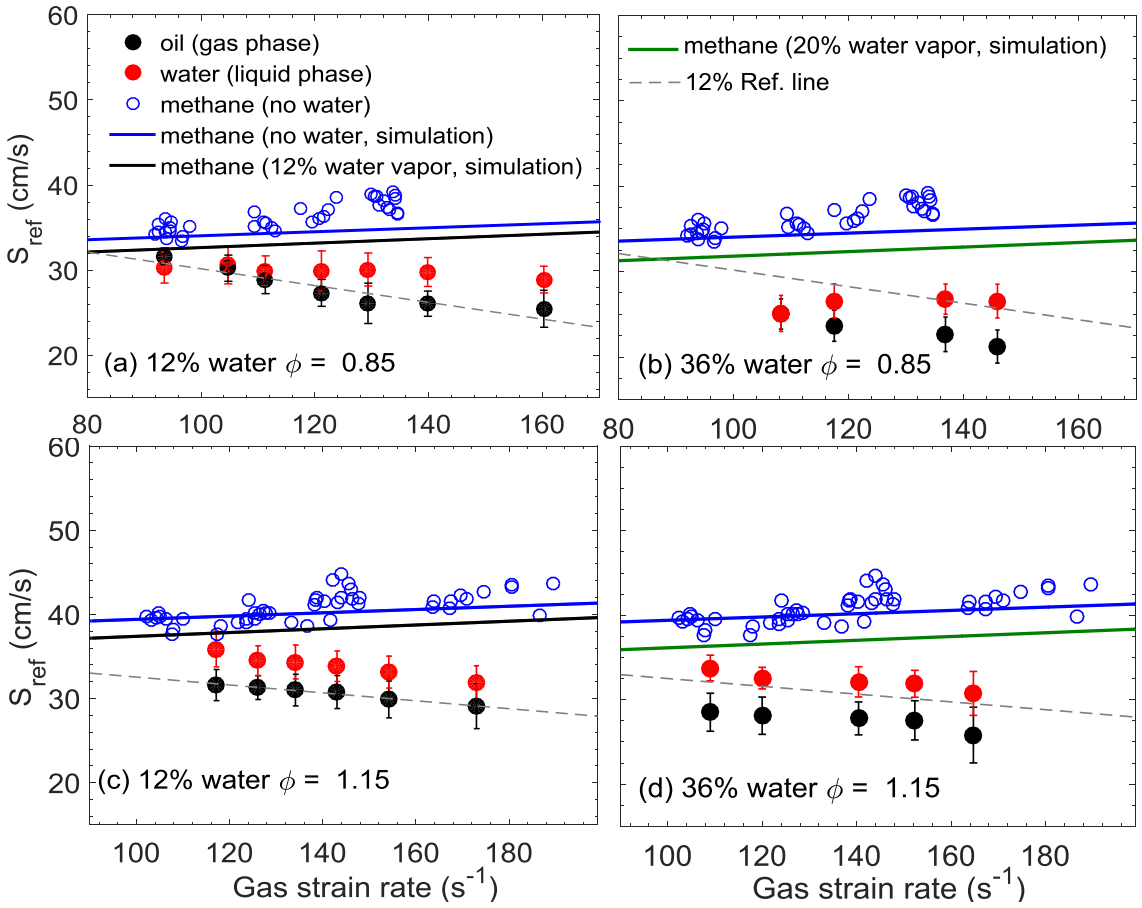

Figure 6: Axial velocity of gas (black circles) and water droplets (red circles) measured at the reference plane of a stretched methane/air/water flame, as a function of gas strain rate. The data for methane flame with no water addition are also plotted (blue circles) as reference. Grey dotted lines are the best linear fit of the flame speed (gas) for 12% water case. Numerical results for methane without water (blue line), and with water vapor addition (black/green lines) are also presented. The legends indicated in (a), (b) apply to all subfigures. Note that in (b) and (d), water vapor cannot be as high as $X_{H_2O(V)}/X_{CH_4} = 36\%$ at room temperature (293 K), so the dewpoint value (20%) is used instead.

addition for the same mass fraction in the gas phase. Simulations of strained flames were made using Cosilab (Rotexo) with GRI-Mech 3.0 as the chemical mechanism. Details on this counterflow modelling can be found in [14]. The same mechanism for water vapor addition to methane flames has been validated by Mazas *et al.* [15]. The same approach was used to extract reference flame speed and strain rate from the simulation results. The results are plotted in the same figure (Fig. 6) for 12% and 20% [b] molar water/methane addition. Simulations for 36% ratio are not possible, since at room temperature (293 K) the dewpoint value corresponds to $X_{H_2O}/X_{CH_4} = 20\%$. The numerical results match well with the experimental data for the water-free cases. However, the model predicts only a slight drop in the flame speed with the addition of water vapor, compared with the significant flame speed reduction in the droplet cases measured at the same strain rate. In contrast to the experiment, the addition of water vapor does not change the gradient of the flame speed slope. The comparison with numerical results on water vapor addition suggests that the physical properties and dynamics of water droplets (large latent heat of vaporization and inertia) have a greater influence than the direct role via heat capacity or chemical influence [16, 17].

6. Conclusions

The effect of water droplets on a strained laminar flame was investigated by measuring the corresponding reference velocities ahead of the flame using two-phase PIV. Measurements of the gas and droplet velocities are made possible by seeding micron-sized oil droplets into the mixture and using an image segmentation tech-

[b]The corresponding water mass fractions for the two simulation cases are 0.008 and 0.012, respectively.

nique. Validation stages for the the technique were performed against gas phase only results to demonstrate accuracy. Measured gas-liquid slip velocities were more pronounced with the rate of deceleration in strained flames.

Reference flame speeds measured as the minimum speed ahead of the flame were determined for both gas phase and water droplets. The reference flame speeds were determined as a function of gas strain rate (100-200 s^{-1}) for molar water droplet/methane ratios of 0, 12 and 36%. Measured droplet reference speeds were up to 10-30% higher than the gas phase velocities, as inertia dominated the droplet motion. In all cases, as expected, reference flame speeds decreased with the addition of water droplets by fractions up to 37%. Gas phase simulations including vaporized water at 12% and 20% water/methane molar fractions show only modest decreases in the reference flame speed. This result means that the role of the heat of vaporization needs to be taken into account to explain the observations. Modifications to the simulation are currently underway to allow the calculations of droplet-laden strained flames in Cosilab.

Acknowledgments

The authors gratefully acknowledge the financial support from Newton Advanced Fellowship (NA160115). Additional funding was provided by a subcontract from Universiti Teknologi Malaysia.

References

[1] S. P. Fuss, E. F. Chen, W. Yang, R. J. Kee, B. A. Williams, J. W. Fleming, Inhibition of premixed methane/air flames by water mist, Proceedings of the Combustion Institute 29 (2002) 361–368.

[2] A. Yoshida, T. Udagawa, Y. Momomoto, H. Naito, Y. Saso, Experimental study of suppressing effect of fine water droplets on propane/air premixed flames stabilized in the stagnation flowfield, Fire Safety Journal 58 (2013) 84–91.

[3] H. Chelliah, A. Lazzarini, P. Wanigarathne, G. Linteris, Inhibition of premixed and non-premixed flames with fine droplets of water and solutions, Proceedings of the Combustion Institute 29 (2002) 369–376.

[4] A. Lazzarini, R. H. Krauss, H. K. Chelliah, G. T. Linteris, Extinction conditions of non-premixed flames with fine droplets of water and water/NaOH solutions, Proceedings of the Combustion Institute 28 (2000) 2939–2945.

[5] G. Continillo, W. Sirignano, Counterflow spray combustion modeling, Combustion and Flame 81 (1990) 325–340.

[6] A. M. Lentati, H. K. Chelliah, Dynamics of water droplets in a counterflow field and their effect on flame extinction, Combustion and Flame 115 (1998) 158–179.

[7] H. K. Chelliah, Flame inhibition/suppression by water mist: Droplet size/surface area, flame structure, and flow residence time effects, Proceedings of the Combustion Institute 31 II (2007) 2711–2719.

[8] N. H. Chen, B. Rogg, K. N. Bray, Modelling laminar two-phase counterflow flames with detailed chemistry and transport, Symposium (International) on Combustion (1992).

[9] R. J. Kee, K. Yamashita, H. Zhu, A. M. Dean, The effects of liquid-fuel thermophysical properties, carrier-gas composition, and pressure, on strained opposed-flow non-premixed flames, Combustion and Flame 158 (2011) 1129–1139.

[10] F. N. Egolfopoulos, H. Zhang, Z. Zhang, Wall effects on the propagation and extinction of steady, strained, laminar premixed flames, Combustion and Flame 109 (1997) 237–252.

[11] D. A. Khalitov, E. K. Longmire, Simultaneous two-phase PIV by two-parameter phase discrimination, Experiments in Fluids 32 (2002) 252–268.

[12] L. Fan, D. McGrath, C. T. Chong, M. N. Mohd Jaafar, H. Zhong, S. Hochgreb, Laser-induced incandescence particle image velocimetry (LII-PIV) for two-phase flow velocity measurement, Experiments in Fluids (2018) 156.

[13] L. Fan, C. T. Chong, T. Bo, Y. Zheng, D. McGrath, S. Hochgreb, Laser-induced incandescence particle image velocimetry (LII-PIV) for simultaneous two-phase flame velocity measurement, submitted to Proceedings of the Combustion Institute 38 (2019).

[14] B. Rogg, Response and flamelet structure of stretched premixed methane/air flames, Combustion and Flame 73 (1988) 45 – 65.

[15] A. N. Mazas, B. Fiorina, D. A. Lacoste, T. Schuller, Effects of water vapor addition on the laminar burning velocity of oxygen-enriched methane flames, Combustion and Flame 158 (2011) 2428–2440.

[16] R. Seiser, K. Seshadri, The influence of water on extinction and ignition of hydrogen and methane flames, Proceedings of the Combustion Institute 30 (2005) 407–414.

[17] R. Padilla, D. Escofet-Martin, T. Pham, W. Pitz, D. Dunn-Rankin, Structure and behavior of water-laden ch4/air counterflow diffusion flames, Combustion and Flame 196 (2018) 439 – 451.